IVYSPRING INTERNATIONAL PUBLISHER

Theranostics

2019; 9(24): 7200-7209. doi: 10.7150/thno.39831

Research Paper

Cooperation of endogenous and exogenous reactive oxygen species induced by zinc peroxide nanoparticles to enhance oxidative stress-based cancer therapy

Li-Sen Lin[1,2*], Jun-Feng Wang[3*], Jibin Song[4*], Yijing Liu[2], Guizhi Zhu[2], Yunlu Dai[2], Zheyu Shen[2], Rui Tian[2], Justin Song[2], Zhantong Wang[2], Wei Tang[2], Guocan Yu[2], Zijian Zhou[2], Zhen Yang[2], Tao Huang[5], Gang Niu[2], Huang-Hao Yang[4], Zhi-Yi Chen[1]✉, Xiaoyuan Chen[2]✉

1. Department of Ultrasound Medicine, Laboratory of Ultrasound Molecular Imaging, the Third Affiliated Hospital of Guangzhou Medical University, Guangzhou 510150, China
2. Laboratory of Molecular Imaging and Nanomedicine (LOMIN), National Institute of Biomedical Imaging and Bioengineering (NIBIB), National Institutes of Health (NIH), Bethesda, Maryland 20892, United States
3. Department of Ultrasound, the First Affiliated Hospital of Harbin Medical University, Harbin, Heilongjiang 150076, China
4. MOE Key Laboratory for Analytical Science of Food Safety and Biology, College of Chemistry, Fuzhou University, Fuzhou 350108, China
5. Department of Radiology, the Fourth Hospital of Harbin Medical University, Harbin, Heilongjiang 150076, China

*These authors contributed equally to this work.

✉ Corresponding authors: Zhi-Yi Chen (winchen@vip.126.com), Xiaoyuan Chen (shawn.chen@nih.gov)

Received: 2019.08.31; Accepted: 2019.09.04; Published: 2019.09.23

Abstract

Reactive oxygen species (ROS)-generating anticancer agents can act through two different mechanisms: (i) elevation of endogenous ROS production in mitochondria, or (ii) formation/delivery of exogenous ROS within cells. However, there is a lack of research on the development of ROS-generating nanosystems that combine endogenous and exogenous ROS to enhance oxidative stress-mediated cancer cell death.

Methods: A ROS-generating agent based on polymer-modified zinc peroxide nanoparticles (ZnO_2 NPs) was presented, which simultaneously delivered exogenous H_2O_2 and Zn^{2+} capable of amplifying endogenous ROS production for synergistic cancer therapy.

Results: After internalization into tumor cells, ZnO_2 NPs underwent decomposition in response to mild acidic pH, resulting in controlled release of H_2O_2 and Zn^{2+}. Intriguingly, Zn^{2+} could increase the production of mitochondrial $O_2^{\cdot -}$ and H_2O_2 by inhibiting the electron transport chain, and thus exerted anticancer effect in a synergistic manner with the exogenously released H_2O_2 to promote cancer cell killing. Furthermore, ZnO_2 NPs were doped with manganese *via* cation exchange, making them an activatable magnetic resonance imaging contrast agent.

Conclusion: This study establishes a ZnO_2-based theranostic nanoplatform which achieves enhanced oxidative damage to cancer cells by a two-pronged approach of combining endogenous and exogenous ROS.

Key words: reactive oxygen species, zinc peroxide nanoparticles, pH-responsiveness, magnetic resonance imaging, cancer therapy

Introduction

Reactive oxygen species (ROS) including hydrogen peroxide (H_2O_2), superoxide anion radical ($O_2^{\cdot -}$), singlet oxygen, and hydroxyl radical can damage lipids, proteins, and DNA, which would lead to cell death when the ROS level exceeds the cellular antioxidant capacity, a condition referred to as oxidative stress [1-6]. Cells constantly generate endogenous ROS as by-products of aerobic metabolism in mitochondria, and maintain redox homeostasis by controlling the balance between ROS formation and scavenging [7]. More importantly, it has been found that cancer cells show elevated mitochondrial ROS production due to oncogenic stimulation and active metabolism [8-10]. Even though cancer cells enhance antioxidant capacity to counterbalance the overproduction of ROS, their ROS levels are still closer to the toxicity threshold than that of normal cells, making them more susceptible to further ROS formation induced by exogenous agents [11,12]. Therefore, the development of ROS-generating agents that can effectively raise intracellular ROS levels above the toxicity threshold and cause oxidative stress-mediated cell death would be of great interest in cancer therapy.

There are two possible working mechanisms for ROS-generating anticancer agents: (i) enhancement of endogenous ROS production, and (ii) formation/delivery of exogenous ROS. On the one hand, it is well known that mitochondria are the main source of endogenous ROS, and that inhibition of mitochondrial electron transport chain (ETC) can promote the production of $O_2^{\cdot -}$ and H_2O_2 by increasing leakage of electrons to oxygen (O_2) at complexes I and III of the ETC [13,14]. Therefore, several ETC inhibitors have been used to kill tumor cells through endogenous ROS-mediated apoptosis [15]. On the other hand, anticancer agents with exogenous ROS-generating ability, such as photodynamic and sonodynamic sensitizers, are attracting more and more attention [16-21]. In particular, stimuli-responsive nanoplatforms have been actively explored for the formation of exogenous ROS in tumor cells [22-28]. However, to the best of our knowledge, there is a paucity of studies regarding the design of ROS-generating nanosystems that combine endogenous and exogenous ROS to potentiate oxidative stress-induced cancer cell death.

Herein, we report a novel ROS-generating agent based on zinc peroxide nanoparticles (ZnO_2 NPs), which simultaneously delivers exogenous H_2O_2 and Zn^{2+} with the capability of intensifying endogenous ROS production for synergistic cancer therapy (Figure 1). The ZnO_2 NPs were stable at neutral pH but decomposed to Zn^{2+} and H_2O_2 at mild acidic pH. In fact, it has been proved that zinc exerts its antitumor effects through inhibition of ETC and consequent elevation of mitochondrial ROS production [29-34]. As compared to conventional zinc ionophores that have been utilized to increase Zn^{2+} accumulation in cancer cells [35-37], controlled Zn^{2+} delivery systems possess the potential for providing desirable therapeutic outcomes with reduced side effects. In addition, although formation of exogenous H_2O_2 within cells has been recognized as a promising strategy for tumor therapy [38,39], there has been little work on the preparation of H_2O_2-releasing systems with stimuli-responsive property. With these considerations in mind, we designed and synthesized poly(vinylpyrrolidone) (PVP)-modified ZnO_2 NPs as a pH-triggered ROS-generating agent. Upon internalization in tumor cells, ZnO_2 NPs would release exogenous H_2O_2 and Zn^{2+} able to promote endogenous ROS production in mitochondria, which functioned in a synergistic manner to enhance oxidative stress-based cancer cell killing. The vulnerability of tumor cells to additional ROS and the pH-responsiveness of ZnO_2 NPs enabled this ZnO_2-based ROS-generating anticancer agent to achieve good therapeutic efficacy with low side effects. Moreover, the ZnO_2 NPs was successfully doped with paramagnetic manganese (Mn) *via* a cation-exchange method. The pH-stimulated Mn^{2+} release during the decomposition of Mn-doped ZnO_2 (Mn-ZnO_2) NPs endowed them with activatable magnetic resonance imaging (MRI) contrast ability, which is useful to monitor the dissociation of ZnO_2 NPs as well as the subsequent therapeutic process. This study not only highlights the great potential of ZnO_2 nanomaterials in cancer theranostics, but also provides a paradigm for designing stimuli-responsive ROS-generating nanoagents that exacerbate oxidative damage to cancer cells through collaboration between endogenous and exogenous ROS.

Figure 1. Schematic illustration of theranostic ZnO_2 NPs for MRI and enhanced oxidative stress-based cancer therapy. Upon endocytosis by tumor cells, ZnO_2 NPs undergo dissociation in response to mild acidic pH, causing the release of H_2O_2 and Zn^{2+}. The exogenously released H_2O_2 and Zn^{2+}, that can increase the production of mitochondrial $O_2^{\cdot -}$ and H_2O_2 by inhibiting the electron transport chain (ETC), act synergistically to promote cancer cell killing through the cooperation of endogenous and exogenous ROS. Moreover, Mn-doping *via* partial cation exchange imparts ZnO_2 NPs with pH-activated MRI contrast ability.

Materials and methods

Materials

Zinc acetate ($Zn(OAc)_2$, 99.99%), polyvinylpyrrolidone (PVP, Mw = 10000), hydrogen peroxide (H_2O_2, 30 wt. % in H_2O), manganese(II) chloride ($MnCl_2$, 99%), zinc chloride ($ZnCl_2$, 99.999%), zinc oxide nanoparticles (ZnO NPs, 20 wt. % in H_2O), zinquin ethyl ester (95%), 3-(*N*-morpholino)propanesulfonic acid (MOPS, 99.5%), sodium acetate (99%), acetic acid (99.7%), 2′,7′-dichlorofluorescin diacetate (DCFH-DA, 97%), thiazolyl blue tetrazolium bromide (MTT, 97.5%), and propidium iodide (PI, 94%) were purchased from Sigma-Aldrich. Apoptosis kit with annexin V-FITC and PI, hydrogen peroxide assay kit, and calcein-AM were obtained from Fisher Scientific.

Synthesis of PVP-modified ZnO_2 NPs

0.1 g of $Zn(OAc)_2$ and 0.1 g of PVP were dissolved in 5.0 mL of water. Then, 0.5 mL of H_2O_2 was added quickly with vigorous stirring. After reaction for 24 h, the resulting PVP-modified ZnO_2 NPs were washed several times and then re-dispersed in water.

Synthesis of Mn-ZnO_2 NPs

The Mn-doping was achieved by a cation-exchange approach. Briefly, the aqueous solution of ZnO_2 NPs was mixed with the same volume of $MnCl_2$ with different Mn concentrations. After stirring at room temperature for 4 h, the obtained Mn-ZnO_2 NPs were collected by centrifugation (15000 rpm, 15 min).

Decomposition of ZnO_2 NPs

The release of Zn^{2+} and H_2O_2 from ZnO_2 NPs was determined by dialysis. The aqueous solution of ZnO_2 NPs was dialyzed against acetate buffer (pH 5.5) or MOPS buffer (pH 7.4). The Zn^{2+} was measured by inductively coupled plasma optical emission spectrometry (ICP-OES) and the H_2O_2 was measured by using a hydrogen peroxide assay kit.

Intracellular release of Zn^{2+}

Zinquin ethyl ester, a cell-permeable fluorescent probe for Zn^{2+}, was used to evaluate intracellular Zn^{2+} release. After incubation with ZnO_2 NPs for 4 h, U87MG cells were stained with 25 μM zinquin ethyl ester at 37 °C for 30 min. Then, the fluorescence images were collected by an Olympus IX81 fluorescence microscope.

Oxidative stress assessment

Intracellular oxidative stress was determined by using DCFH-DA as a probe. U87MG cells seeded in 6-well plates (2×10^5 cells/well) were exposed to H_2O_2, $ZnCl_2$, H_2O_2 plus $ZnCl_2$, or ZnO_2 NPs for 4 h. After staining with 10 μM DCFH-DA at 37 °C for 30 min, the fluorescence images were obtained.

In vitro cancer therapy

To demonstrate the synergistic anticancer effect of Zn^{2+} and H_2O_2, U87MG cells (5×10^3 cells/well) seeded in 96-well plates were incubated with H_2O_2, $ZnCl_2$, or H_2O_2 plus $ZnCl_2$ (molar ratio, 1:1) for 24 h. Then, the cell viability was measured by MTT assay. Similarly, the *in vitro* anticancer activity of PVP-modified ZnO_2 NPs was examined.

Magnetic resonance imaging

To confirm the pH-activated MRI contrast effect, the Mn-ZnO_2 NPs were dispersed in different buffer solutions for 4 h, and then the samples were imaged by an MRI scanner. For *in vivo* MRI, U87MG tumor-bearing mice were injected with Mn-ZnO_2 NPs (200 μL, [Mn] = 1 mM) through the tail vein. Then, the T_1-weighted MRI images were obtained by an MRI scanner.

In vivo tumor growth inhibition

Mice bearing U87MG tumors (~50 mm^3) were injected intravenously with different formulations every other day for four doses, including (1) saline, (2) H_2O_2, (3) $ZnCl_2$, and (4) ZnO_2 NPs. Each dose of H_2O_2: 0.05 mmol/kg, $ZnCl_2$: 0.05 mmol/kg, ZnO_2 NPs: 5 mg/kg. The tumor volume and body weight of each mouse were recorded every 2 days.

Results and discussion

The ZnO_2 NPs were fabricated by reacting zinc acetate with H_2O_2 in the presence of PVP at room temperature for 24 h. As shown in the transmission electron microscopy (TEM) image (Figure 2A), the as-prepared ZnO_2 NPs had a uniform particle size of about 50 nm. Dynamic light scattering (DLS) results revealed that the average hydrodynamic diameter of ZnO_2 NPs was ~66.1 nm (Figure 2B). In contrast to zinc oxide nanoparticles (ZnO NPs), ZnO_2 NPs exhibited a strong band at 840 cm^{-1} in the Raman spectra assigned to O-O stretching vibration (Figure 2C) [40], clearly demonstrating the existence of peroxide ions (O_2^{2-}). Moreover, the successful synthesis of ZnO_2 NPs was further confirmed by X-ray photoelectron spectroscopy (XPS). An O 1s peak with binding energy of 532 eV corresponding to O_2^{2-} was observed for the ZnO_2 NPs, whereas the O 1s peak of ZnO NPs was located at 530 eV attributed to O^{2-} (Figure 2D, Figure S1) [41].

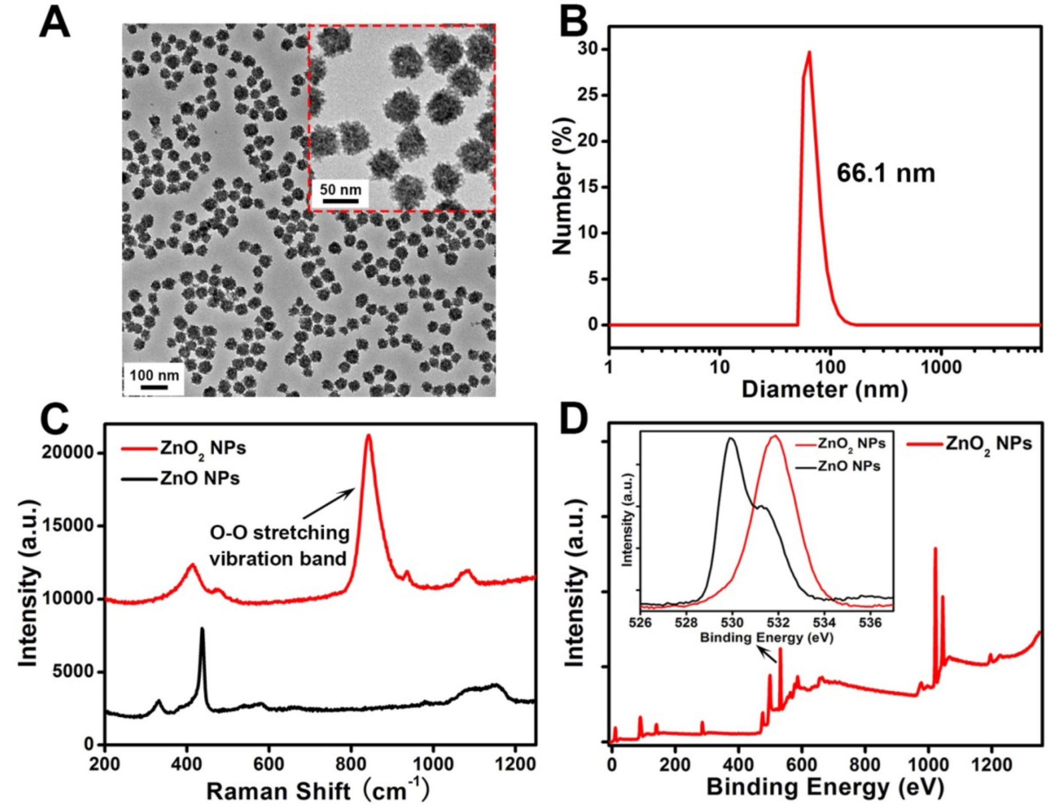

Figure 2. (A) TEM image and (B) DLS data of ZnO_2 NPs. (C) Raman spectra of ZnO NPs and ZnO_2 NPs. (D) XPS survey spectra and O 1s peak (inset) of ZnO_2 NPs.

To demonstrate the pH-dependent dissociation behavior of ZnO_2 NPs, we measured the release of Zn^{2+} and H_2O_2 from ZnO_2 NPs under neutral (pH 7.4) or acidic (pH 5.5) conditions. It can be seen in Figure 3A,B that both Zn^{2+} and H_2O_2 were gradually released from the ZnO_2 NPs at pH 5.5. In contrast, the release rates were relatively slow in pH 7.4 buffer solution. As shown by TEM (Figure 3C), ZnO_2 NPs were stable at pH 7.4 but degraded at pH 5.5. Thus, the accelerated release in mild acidic environment can be ascribed to the pH-responsive degradation of ZnO_2 NPs, which is favorable for *in vivo* tumor treatment since the acidic endo/lysosomes (pH 5.0-6.0) of cancer cells can trigger the release of H_2O_2 and Zn^{2+} on demand. Then, the decomposition of ZnO_2 NPs in cancer cells was confirmed by evaluating the intracellular release of Zn^{2+} with a cell-permeable fluorescent Zn^{2+} probe, zinquin ethyl ester [42-45]. As expected, ZnO_2 NPs-incubated U87MG cancer cells exhibited stronger blue fluorescence than control untreated cells, and the blue fluorescence increased with increasing concentration of ZnO_2 NPs (Figure 3D, Figure S2), demonstrating the intracellular degradation of ZnO_2 NPs.

To determine whether Zn^{2+} and H_2O_2 could exert anticancer activity in a synergistic manner, we assessed their ability to induce oxidative stress and cytotoxicity. First, the intracellular oxidative stress caused by H_2O_2 or Zn^{2+} was examined by employing 2′,7′-dichlorofluorescin diacetate (DCFH-DA) as the probe. After being deacetylated by cellular esterases, DCFH-DA is converted to DCFH that can interact with ROS to generate fluorescent 2′,7′-dichlorofluorescein (DCF) [46-51]. As shown in Figure 4A, U87MG cells incubated with either H_2O_2 or $ZnCl_2$ displayed significantly greater DCF fluorescence compared with untreated control cells, implying the occurrence of oxidative stress in cancer cells upon H_2O_2 or Zn^{2+} exposure. The Zn^{2+}-dependent oxidative stress could be mainly attributed to the increased mitochondrial ROS production [29-34]. Moreover, the DCF fluorescence in U87MG cells co-incubated with H_2O_2 and $ZnCl_2$ was higher than that in cells incubated with H_2O_2 or $ZnCl_2$ alone, which indicated the combined effect of H_2O_2 and Zn^{2+} on amplification of oxidative stress. The oxidative stress-mediated cytotoxicity of H_2O_2 and Zn^{2+} was further evaluated by MTT assay. As expected, both H_2O_2 and $ZnCl_2$ exhibited concentration-dependent toxicity (Figure 4B). More importantly, the viability of U87MG cells co-treated with H_2O_2 and $ZnCl_2$ at a molar ratio of 1:1 was lower than that of cells treated with $ZnCl_2$ or H_2O_2 alone, demonstrating the synergistic anticancer effect of H_2O_2 and Zn^{2+}. It has been reported that mitochondria, one of the most important organelles responsible for energy metabolism, are particularly vulnerable to oxidative damage as they are constantly exposed to high levels of endogenous ROS [52]. Therefore, the synergy between H_2O_2 and Zn^{2+} is probably because large amount of exogenously released H_2O_2 is able to disturb cellular redox homeostasis and then the enhanced mitochondrial ROS production resulting from inhibition of ETC by Zn^{2+} can lead to the impairment of mitochondria. These results suggested that exogenous H_2O_2 and Zn^{2+} with the capability of promoting endogenous ROS production could function cooperatively to enhance oxidative stress-induced tumor cell death.

Next, the *in vitro* anticancer effect of PVP-modified ZnO_2 NPs was examined. As can be seen in Figure 5A, the PVP-modified ZnO_2 NPs exerted remarkable therapeutic efficacy against cancer cells, which could be ascribed to the pH-responsive release of H_2O_2 and Zn^{2+} from ZnO_2 NPs in acidic endo/lysosomes and the subsequent occurrence of oxidative stress (Figure 5B). In addition, ZnO_2 NPs exhibited a time- and dose-dependent cytotoxicity (Figure S3). To further confirm ZnO_2 NPs-caused cancer cell death, the fluorescent indicators calcein-AM and propidium iodide (PI) were used to stain live (green) and dead (red) cells, respectively. Effective cell killing was observed when U87MG cells were exposed to ZnO_2 NPs for 24 h (Figure 5C). The oxidative stress-triggered cancer cell apoptosis was then determined by annexin V-FITC/PI apoptosis detection kit. As shown in flow cytometry profiles (Figure 5D, Figure S4), U87MG cells underwent apoptosis after treatment with ZnO_2 NPs for 12 h. Furthermore, the percentage of apoptotic cancer cells increased with increasing dose of ZnO_2 NPs. The above results demonstrated the potential of pH-responsive ZnO_2 NPs as an efficient therapeutic agent to cause oxidative stress and cancer cell apoptosis.

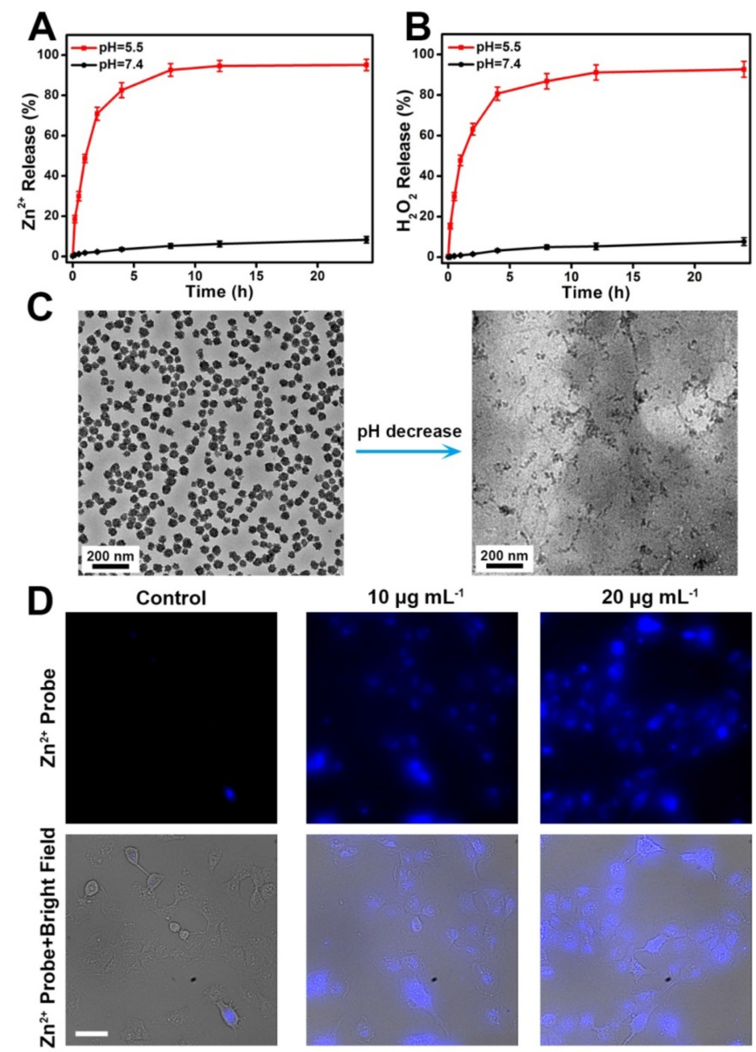

Figure 3. Release profiles of (A) Zn^{2+} and (B) H_2O_2 from ZnO_2 NPs at different pH values. (C) TEM images of ZnO_2 NPs after 2 h of incubation in pH 7.4 (left) and pH 5.5 (right) buffer solutions. (D) Fluorescence images of zinquin ethyl ester-stained U87MG cells after incubation with different concentration of ZnO_2 NPs for 4 h. Scale bar, 50 μm.

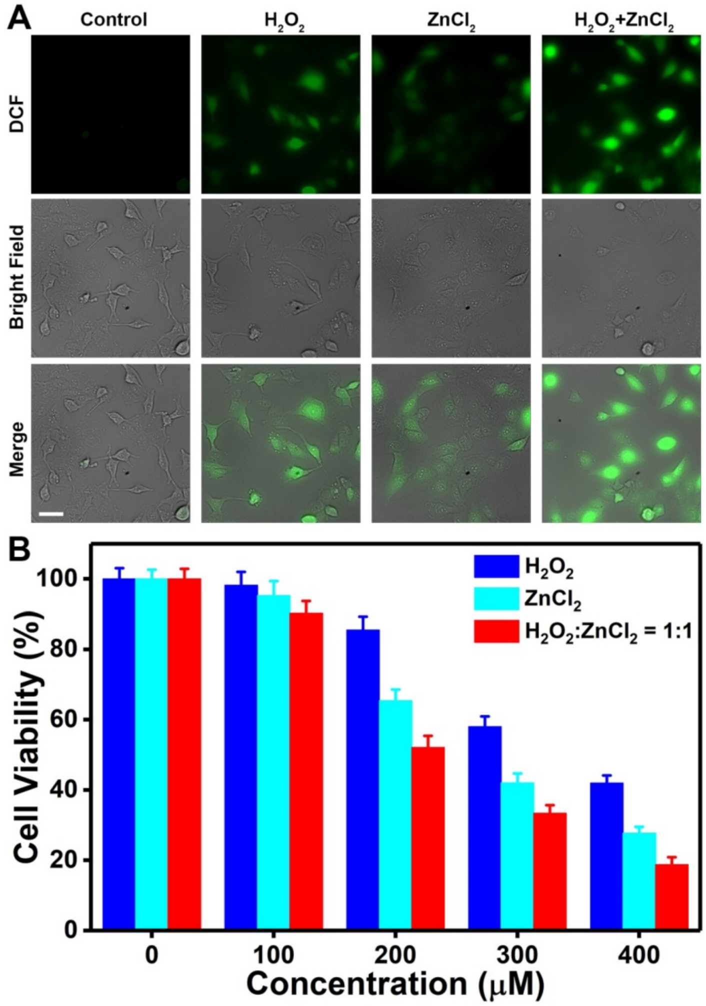

Figure 4. (A) DCF fluorescence of U87MG cells after different treatments. [H_2O_2] = 200 μM, [$ZnCl_2$] = 200 μM. Scale bar, 50 μm. (B) Cell viability after 24 h of exposure to H_2O_2, $ZnCl_2$, or H_2O_2 plus $ZnCl_2$ (molar ratio, 1:1).

Theranostic agents that integrate diagnostic and therapeutic functions into a single nanoplatform offer great opportunities for personalized cancer treatment [53-59]. In order to endow ZnO_2 NPs with MRI contrast ability, a facile cation-exchange strategy was employed for the construction of Mn-doped ZnO_2 NPs (Figure 6A). The multifunctional Mn-ZnO_2 NPs were synthesized by mixing ZnO_2 NPs with different amounts of $MnCl_2$ at room temperature for 4 h. An obvious color change was observed after treatment of ZnO_2 NPs with $MnCl_2$ (Figure S5). Importantly, there was no distinct morphology difference between ZnO_2 and Mn-ZnO_2 NPs when the weight fraction of Mn was 6.5% or below (Figure S6). The Mn-ZnO_2 NPs with 6.5% of Mn were thus selected for the following studies. Moreover, the energy-dispersive X-ray spectroscopy (EDS) and EDS mapping data also verified the successful fabrication of Mn-ZnO_2 NPs (Figure 6B, Figure S7).

Inspired by the pH-dependent dissolution behavior of ZnO_2 NPs, we compared the longitudinal (T_1) relaxivity of Mn-ZnO_2 NPs dispersed in buffer solutions with different pH values. Intriguingly, the T_1 relaxation rate (r_1) value increased from 0.59 to 4.68 mM^{-1} s^{-1} as the pH decreased from 7.4 to 5.5 (Figure 6C, Figure S8), revealing the pH-activated MRI contrast performance of Mn-ZnO_2 NPs. Such an activatable T_1 contrast effect is mainly due to the fact that pH-stimulated release of Mn^{2+} from Mn-ZnO_2 NPs provides more efficient chemical exchange between Mn^{2+} ions and protons. The off-to-on contrast ability in response to specific stimuli makes Mn-ZnO_2 NPs highly promising for tumor MRI *in vivo*. To verify this, U87MG tumor-bearing mice were injected with Mn-ZnO_2 NPs through the tail vein and then imaged by an MRI scanner. As shown in Figure 6D, positive contrast effect was found at the tumor site after intravenous administration of Mn-ZnO_2 NPs. Furthermore, the MRI T_1 signal in the tumor region gradually increased with time, which could be attributed to the high tumor uptake of Mn-ZnO_2 NPs. These results indicated that Mn-ZnO_2 NPs is a promising MRI contrast agent for cancer imaging.

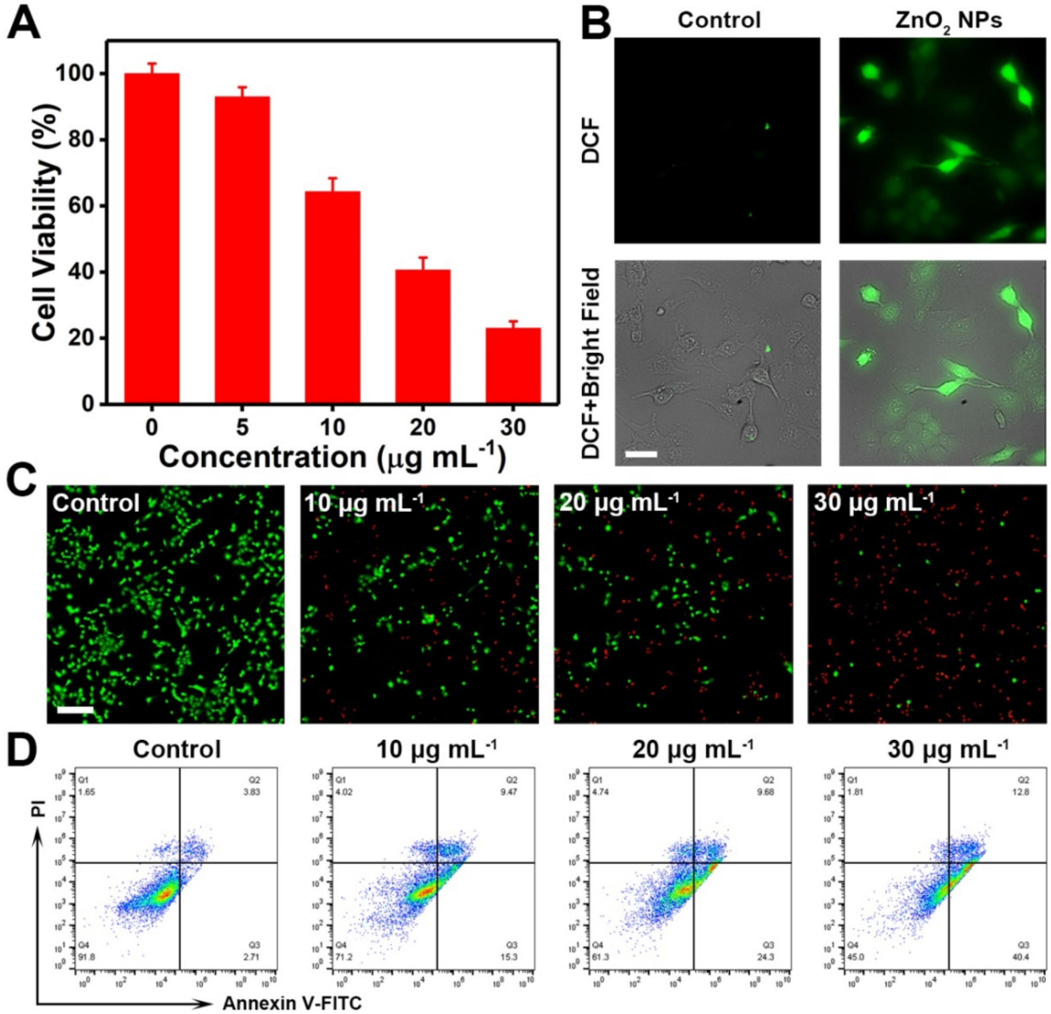

Figure 5. (A) *In vitro* anticancer activity of ZnO_2 NPs after 24 h of incubation. (B) DCF fluorescence of U87MG cells after 4 h of incubation with 10 μg mL^{-1} ZnO_2 NPs. Scale bar, 50 μm. (C) Calcein-AM (green, live cells) and PI (red, dead cells) co-stained fluorescence images of cells treated with different concentrations of ZnO_2 NPs for 24 h. Scale bar, 100 μm. (D) Flow cytometry data showing apoptosis in U87MG cells after exposure to ZnO_2 NPs for 12 h.

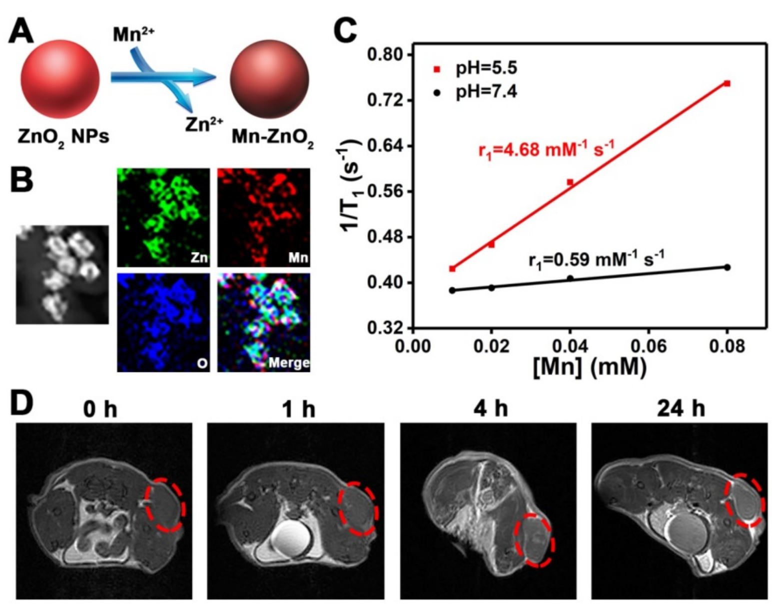

Figure 6. (A) Scheme showing the preparation of Mn-doped ZnO_2 NPs through a facile cation-exchange approach. (B) EDS mapping of Mn-ZnO_2 NPs. (C) The r_1 values of Mn-ZnO_2 NPs under different pH conditions. (D) T_1-weighted MRI of U87MG tumor-bearing mice after intravenous injection of Mn-doped ZnO_2 NPs. The red circles indicate the tumor area.

In view of the potent anticancer activity of PVP-modified ZnO_2 NPs *in vitro*, we further investigated their feasibility for inhibiting tumor growth *in vivo*. Mice bearing U87MG tumors were treated with different formulations by intravenous injection, and tumor size was measured every other day using a caliper. As can be seen in Figure 7A, the growth of tumors in mice injected with ZnO_2 NPs was significantly suppressed, demonstrating the high therapeutic efficacy of ZnO_2-based oxidative stress inducers. In comparison, both H_2O_2 and $ZnCl_2$ showed only limited tumor growth inhibition (Figure S9), most likely due to the rapid clearance after intravenous administration. Moreover, no significant body weight loss was observed after various treatments (Figure 7B,C). Hematoxylin and eosin (H&E)-stained images of major organs collected from different groups of mice at day 14 showed no obvious organ injury (Figure S10). Then, the oxidative stress-stimulated cancer cell apoptosis was determined by terminal deoxynucleotidyl transferase-mediated dUTP nick-end labeling (TUNEL) assay. Tumor tissues derived from mice treated with ZnO_2 NPs had significantly more apoptotic cells as compared to that from saline-injected mice (Figure 7D). In addition, H&E staining indicated that tumors in ZnO_2 NPs-treated mice exhibited severe damage (Figure 7E). The above results suggested that ZnO_2 NPs are good candidates for cancer treatment *in vivo*.

Conclusions

In summary, we have successfully developed a ZnO_2 NPs-based ROS-generating nanoagent that enhances oxidative stress-mediated cancer cell killing through the collaboration of endogenous and exogenous ROS, and demonstrated its use in the fabrication of activatable theranostic nanoplatform for MRI-guided tumor treatment. After uptake by cancer cells, the pH-responsive ZnO_2 NPs, in addition to releasing exogenous H_2O_2, also provide Zn^{2+} to facilitate the production of endogenous $O_2^{\cdot -}$ and H_2O_2 from mitochondrial ETC, enabling highly effective synergistic tumor therapy. The pH-dependent dissociation behavior of ZnO_2 NPs, together with the fact that cancer cells are more vulnerable to additional ROS than normal cells, allows them to efficiently trigger cell apoptosis in tumor and show negligible

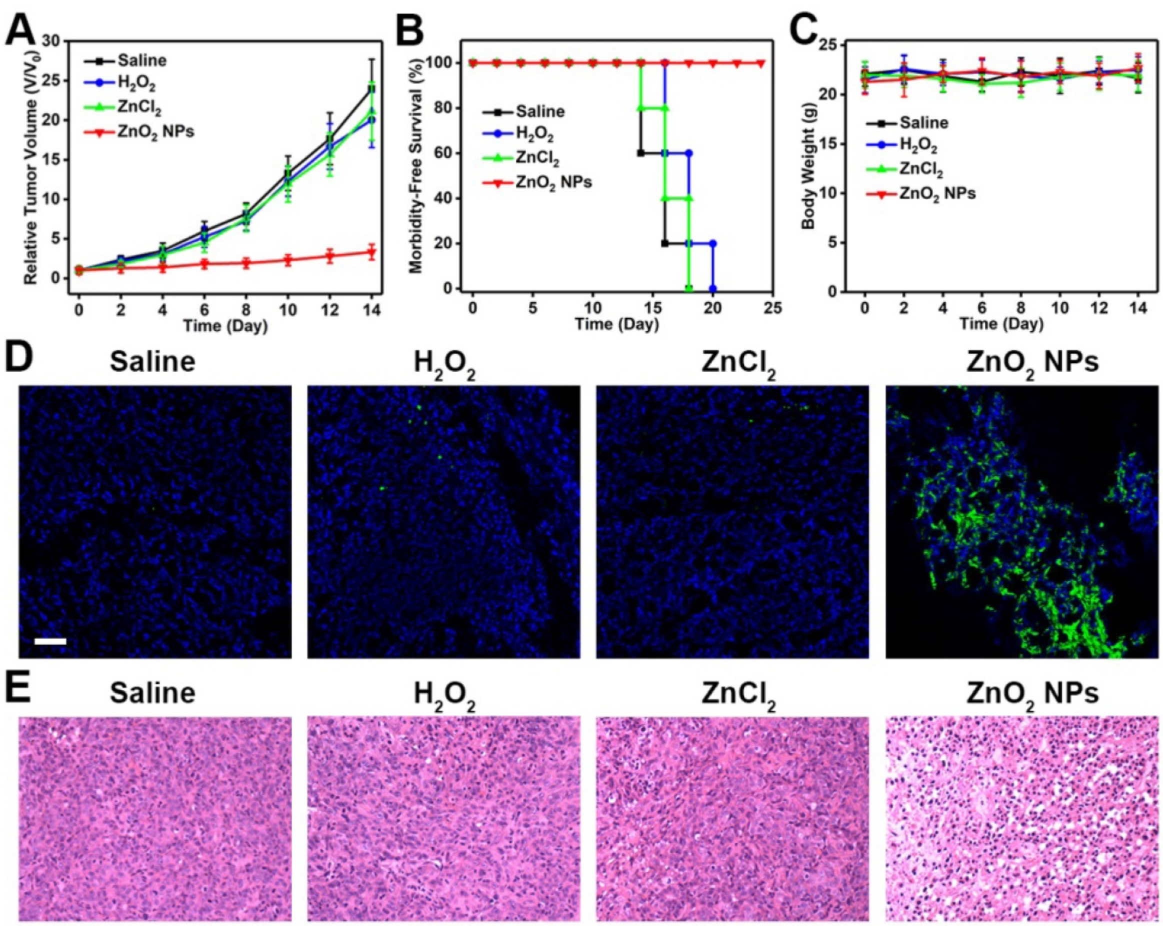

Figure 7. (A) Tumor growth curves of U87-bearing mice injected intravenously with different formulations. (B) Survival curves of mice in different groups. (C) Body weight changes of mice during the observation period. (D) TUNEL and (E) H&E staining of tumor tissues derived from different groups. Scale bar in d, 50 μm.

damage to major organs. Moreover, manganese could be easily doped into ZnO_2 NPs by cation exchange to impart them with pH-activated MRI contrast property, which is appropriate for monitoring the dissolution of ZnO_2 NPs and subsequent therapeutic process. Our study not only demonstrates the utilization of ZnO_2 nanomaterials for theranostic applications, but also provides a two-pronged strategy to further improve oxidative stress-based cancer therapy by stimulating cooperation between endogenous and exogenous ROS.

Abbreviations

ROS: Reactive oxygen species; ZnO_2 NPs: zinc peroxide nanoparticles; H_2O_2: hydrogen peroxide; $O_2^{\bullet-}$: superoxide anion radical; ETC: electron transport chain; PVP: poly(vinylpyrrolidone); MOPS: 3-(N-morpholino)propanesulfonic acid; DCFH-DA: 2′,7′-dichlorofluorescin diacetate; MTT: thiazolyl blue tetrazolium bromide; PI: propidium iodide; Mn-ZnO_2: Mn-doped ZnO_2; MRI: magnetic resonance imaging; TEM: transmission electron microscopy; DLS: dynamic light scattering; XPS: X-ray photoelectron spectroscopy; DCFH-DA: 2′,7′-dichlorofluorescin diacetate; H&E: hematoxylin and eosin; TUNEL: terminal deoxynucleotidyl transferase-mediated dUTP nick-end labeling.

Supplementary Material

Supplementary figures and tables.
http://www.thno.org/v09p7200s1.pdf

Acknowledgements

This work was supported by the National Natural Science Foundation of China (Nos. 81971621, 81671707), Natural Science Foundation of Guangdong Province (No. 2016A030311054), Research Projects of Guangzhou Science Technology and Innovation Commission (No. 201607010201), Research Fund for Lin He’s Academician Workstation of New Medicine and Clinical Translation, Higher Education Colleges and Universities Innovation Strong School Project (Q17024072), and the Intramural Research Program (IRP) of the NIBIB, NIH.

Competing Interests

The authors have declared that no competing interest exists.

References

1. Brynildsen MP, Winkler JA, Spina CS, MacDonald IC, Collins JJ. Potentiating antibacterial activity by predictably enhancing endogenous microbial ROS production. Nat Biotechnol. 2013; 31: 160-5.
2. Ma P, Xiao H, Yu C, Liu J, Cheng Z, Song H, et al. Enhanced cisplatin chemotherapy by iron oxide nanocarrier-mediated generation of highly toxic reactive oxygen species. Nano Lett. 2017; 17: 928-37.
3. Lin LS, Song J, Song L, Ke K, Liu Y, Zhou Z, et al. Simultaneous Fenton-like ion delivery and glutathione depletion by MnO_2-based nanoagent to enhance chemodynamic therapy. Angew Chem Int Ed Engl. 2018; 57: 4902-6.
4. Tang Z, Zhang H, Liu Y, Ni D, Zhang H, Zhang J, et al. Antiferromagnetic pyrite as the tumor microenvironment-mediated nanoplatform for self-enhanced tumor imaging and therapy. Adv Mater. 2017; 29: 1701683.
5. Su X, Shen Z, Yang Q, Sui F, Pu J, Ma J, et al. Vitamin C kills thyroid cancer cells through ROS-dependent inhibition of MAPK/ERK and PI3K/AKT pathways *via* distinct mechanisms. Theranostics. 2019; 9: 4461-73.
6. Zhao J, Gao W, Cai X, Xu J, Zou D, Li Z, et al. Nanozyme-mediated catalytic nanotherapy for inflammatory bowel disease. Theranostics. 2019; 9: 2843-55.
7. Giorgio M, Trinei M, Migliaccio E, Pelicci PG. Hydrogen peroxide: a metabolic by-product or a common mediator of ageing signals? Nat Rev Mol Cell Biol. 2007; 8: 722-8.
8. Trachootham D, Zhou Y, Zhang H, Demizu Y, Chen Z, Pelicano H, et al. Selective killing of oncogenically transformed cells through a ROS-mediated mechanism by β-phenylethyl isothiocyanate. Cancer Cell. 2006; 10: 241-52.
9. Gorrini C, Harris IS, Mak TW. Modulation of oxidative stress as an anticancer strategy. Nat Rev Drug Discovery. 2013; 12: 931-47.
10. Ma X, Ren X, Guo X, Fu C, Wu Q, Tan L, et al. Multifunctional iron-based metal-organic framework as biodegradable nanozyme for microwave enhancing dynamic therapy. Biomaterials. 2019; 214: 119223.
11. Trachootham D, Alexandre J, Huang P. Targeting cancer cells by ROS-mediated mechanisms: a radical therapeutic approach? Nat Rev Drug Discovery. 2009; 8: 579-91.
12. Schumacker PT. Reactive oxygen species in cancer: a dance with the devil. Cancer Cell. 2015; 27: 156-7.
13. Balaban RS, Nemoto S, Finkel T. Mitochondria, oxidants, and aging. Cell. 2005; 120: 483-95.
14. Esposito LA, Melov S, Panov A, Cottrell BA, Wallace DC. Mitochondrial disease in mouse results in increased oxidative stress. Proc Natl Acad Sci USA. 1999; 96: 4820-5.
15. Indo HP, Davidson M, Yen HC, Suenaga S, Tomita K, Nishii T, et al. Evidence of ROS generation by mitochondria in cells with impaired electron transport chain and mitochondrial DNA damage. Mitochondrion. 2007; 7: 106-18.
16. Huang L, Li Z, Zhao Y, Yang J, Yang Y, Pendharkar AI, et al. Enhancing photodynamic therapy through resonance energy transfer constructed near-infrared photosensitized nanoparticles. Adv Mater. 2017; 29: 1604789.
17. Ni D, Ferreira CA, Barnhart TE, Quach V, Yu B, Jiang D, et al. Magnetic targeting of nanotheranostics enhances cerenkov radiation-induced photodynamic therapy. J Am Chem Soc. 2018; 140: 14971-9.
18. Li X, Lee D, Huang JD, Yoon J, Phthalocyanine-assembled nanodots as photosensitizers for highly efficient type I photoreactions in photodynamic therapy. Angew Chem Int Ed Engl. 2018; 57: 9885-90.
19. Ju E, Dong K, Chen Z, Liu Z, Liu C, Huang Y, et al. Copper(II)-graphitic carbon nitride triggered synergy: improved ROS generation and reduced glutathione levels for enhanced photodynamic therapy. Angew Chem Int Ed Engl. 2016; 55: 11467-71.
20. Zheng T, Wang W, Wu F, Zhang M, Shen J, Sun Y. Zwitterionic polymer-gated Au@TiO_2 core-shell nanoparticles for imaging-guided combined cancer therapy. Theranostics 2019; 9: 5035-48.
21. Luby BM, Walsh CD, Zheng G. Advanced photosensitizer activation strategies for smarter photodynamic therapy beacons. Angew Chem Int Ed Engl. 2019; 58: 2558-69.
22. Kolemen S, Ozdemir T, Lee D, Kim GM, Karatas T, Yoon J, et al. Remote-controlled release of singlet oxygen by the plasmonic heating of endoperoxide-modified gold nanorods: towards a paradigm change in photodynamic therapy. Angew Chem Int Ed Engl. 2016; 55: 3606-10.
23. Li WP, Su CH, Chang YC, Lin YJ, Yeh CS. Ultrasound-induced reactive oxygen species mediated therapy and imaging using a Fenton reaction activable polymersome. ACS Nano. 2016; 10: 2017-27.
24. Huo M, Wang L, Chen Y, Shi J. Tumor-selective catalytic nanomedicine by nanocatalyst delivery. Nat Commun. 2017; 8: 357.
25. Wang XQ, Gao F, Zhang XZ. Initiator-loaded gold nanocages as a light-induced free-radical generator for cancer therapy. Angew Chem Int Ed Engl. 2017; 56: 9029-33.
26. Li J, Dirisala A, Ge Z, Wang Y, Yin W, Ke W, et al. Therapeutic vesicular nanoreactors with tumor-specific activation and self-destruction for synergistic tumor ablation. Angew Chem Int Ed Engl. 2017; 56: 14025-30.
27. Wang S, Wang Z, Yu G, Zhou Z, Jacobson O, Liu Y, et al. Tumor-specific drug release and reactive oxygen species generation for cancer chemo/chemodynamic combination therapy. Adv Sci. 2019; 6: 1801986.
28. Zhang M, Shen B, Song R, Wang H, Lv B, Meng X, et al. Radiation-assisted metal ion interference tumor therapy by barium peroxide-based nanoparticles. Mater Horiz. 2019; 6: 1034-40.
29. Kolenko V, Teper E, Kutikov A, Uzzo R. Zinc and zinc transporters in prostate carcinogenesis. Nat Rev Urol. 2013; 10: 219-26.
30. Golovine K, Makhov P, Uzzo RG, Shaw T, Kunkle D, Kolenko VM. Overexpression of the zinc uptake transporter hZIP1 inhibits nuclear factor-kB and reduces the malignant potential of prostate cancer cells *in vitro* and *in vivo*. Clin Cancer Res. 2008; 14: 5376-84.
31. Franklin RB, Costello LC. Zinc as an anti-tumor agent in prostate cancer and in other cancers. Arch Biochem Biophys. 2007; 463: 211-7.

32. Dineley KE, Richards LL, Votyakova TV, Reynolds IJ. Zinc causes loss of membrane potential and elevates reactive oxygen species in rat brain mitochondria. Mitochondrion. 2005; 5: 55-65.
33. Kleiner D. The effect of Zn^{2+} ions on mitochondrial electron transport. Arch Biochem Biophys. 1974; 165: 121-5.
34. Costello LC, Franklin RB. A comprehensive review of the role of zinc in normal prostate function and metabolism; and its implications in prostate cancer. Arch Biochem Biophys. 2016; 611: 100-12.
35. Ding WQ, Liu B, Vaught JL, Yamauchi H, Lind SE. Anticancer activity of the antibiotic clioquinol. Cancer Res. 2005; 65: 3389-95.
36. Magda D, Lecane P, Wang Z, Hu W, Thiemann P, Ma X, et al. Synthesis and anticancer properties of water-soluble zinc ionophores. Cancer Res. 2008; 68: 5318-25.
37. Ding WQ, Yu HJ, Lind SE. Zinc-binding compounds induce cancer cell death *via* distinct modes of action. Cancer Lett. 2008; 271: 251-9.
38. Fang J, Sawa T, Akaike T, Maeda H. Tumor-targeted delivery of polyethylene glycol-conjugated D-amino acid oxidase for antitumor therapy *via* enzymatic generation of hydrogen peroxide. Cancer Res. 2002; 62: 3138-43.
39. Fang J, Deng D, Nakamura H, Akuta T, Qin H, Iyer AK, et al. Oxystress inducing antitumor therapeutics *via* tumor-targeted delivery of PEG-conjugated D-amino acid oxidase. Int J Cancer. 2008; 122: 1135-44.
40. Bai H, Liu X. Green hydrothermal synthesis and photoluminescence property of ZnO_2 nanoparticles. Materials Lett. 2010; 64: 341-3.
41. Dupin JC, Gonbeau D, Vinatier P, Levasseur A. Systematic XPS studies of metal oxides, hydroxides and peroxides. Phys Chem Chem Phys. 2000; 2: 1319-24.
42. Chen WH, Luo GF, Qiu WX, Lei Q, Hong S, Wang SB, et al. Programmed nanococktail for intracellular cascade reaction regulating self-synergistic tumor targeting therapy. Small. 2016; 12: 733-44.
43. Ju E, Chen Z, Li W, Dong K, Wang Z, Liu Z, et al. Embedding magnetic nanoparticles into coordination polymers to mimic zinc ion transporters for targeted tumor therapy. Chem Commun. 2016; 52: 12598-601.
44. He D, He X, Yang X, Li HW. A smart ZnO@polydopamine-nucleic acid nanosystem for ultrasensitive live cell mRNA imaging by the target-triggered intracellular self-assembly of active DNAzyme nanostructures. Chem Sci. 2017; 8: 2832-40.
45. Zhang ZY, Xu YD, Ma YY, Qiu LL, Wang Y, Kong JL, et al. Biodegradable ZnO@polymer core-shell nanocarriers: pH-triggered release of doxorubicin *in vitro*. Angew Chem Int Ed Engl. 2013; 52: 4127-31.
46. Shen S, Zhu C, Huo D, Yang M, Xue J, Xia Y. A hybrid nanomaterial for the controlled generation of free radicals and oxidative destruction of hypoxic cancer cells. Angew Chem Int Ed Engl. 2017; 56: 8801-4.
47. Lin LS, Huang T, Song J, Ou XY, Wang Z, Deng H, et al. Synthesis of copper peroxide nanodots for H_2O_2 self-supplying chemodynamic therapy, J Am Chem Soc. 2019; 141: 9937-45.
48. Noh J, Kwon B, Han E, Park M, Yang W, Cho W, et al. Amplification of oxidative stress by a dual stimuli-responsive hybrid drug enhances cancer cell death. Nat Commun. 2015; 6: 6907.
49. Lin LS, Cong ZX, Li J, Ke KM, Guo SS, Yang HH, et al. Graphitic-phase C_3N_4 nanosheets as efficient photosensitizers and pH-responsive drug nanocarriers for cancer imaging and therapy. J Mater Chem B. 2014; 2: 1031-7.
50. Qi T, Chen B, Wang Z, Du H, Liu D, Yin Q, et al. A pH-activatable nanoparticle for dual-stage precisely mitochondria-targeted photodynamic anticancer therapy. Biomaterials. 2019; 213: 119219.
51. Cheng H, Zheng RR, Fan GL, Fan JH, Zhao LP, Jiang XY, et al. Mitochondria and plasma membrane dual-targeted chimeric peptide for single-agent synergistic photodynamic therapy. Biomaterials. 2019; 188: 1-11.
52. Szeto HH. Cell-permeable, mitochondrial-targeted, peptide antioxidants. AAPS J. 2006; 8: E277.
53. Lin LS, Yang X, Zhou Z, Yang Z, Jacobson O, Liu Y, et al. Yolk-shell nanostructure: an ideal architecture to achieve harmonious integration of magnetic-plasmonic hybrid theranostic platform. Adv Mater. 2017; 29: 1606681.
54. Ke K, Yang W, Xie X, Liu R, Wang LL, Lin WW, et al. Copper manganese sulfide nanoplates: a new two-dimensional theranostic nanoplatform for MRI/MSOT dual-modal imaging-guided photothermal therapy in the second near-infrared window. Theranostics. 2017; 7: 4763-76.
55. Lin LS, Song J, Yang HH, Chen X. Yolk-shell nanostructures: design, synthesis, and biomedical applications. Adv Mater. 2018; 30: 1704639.
56. Hameed S, Bhattarai P, Liang X, Zhang N, Xu Y, Chen M, et al. Self-assembly of porphyrin-grafted lipid into nanoparticles encapsulating doxorubicin for synergistic chemo-photodynamic therapy and fluorescence imaging. Theranostics. 2018; 8: 5501-18.
57. Wang S, Zhou Z, Wang Z, Liu Y, Jacobson O, Shen Z, et al. Gadolinium metallofullerene-based activatable contrast agent for tumor signal amplifcation and monitoring of drug release. Small. 2019; 15: 1900691.
58. Lin LS, Cong ZX, Cao JB, Ke KM, Peng QL, Gao J, et al. Multifunctional Fe_3O_4@polydopamine core-shell nanocomposites for intracellular mRNA detection and imaging-guided photothermal therapy. ACS Nano. 2014; 8: 3876-83.
59. Huang H, Lovell JF. Advanced functional nanomaterials for theranostics. Adv Funct Mater. 2017; 27: 1603524.